Т. 86, № 5 **ЖУРНАЛ ПРИКЛАДНОЙ СПЕКТРОСКОПИИ** СЕНТЯБРЬ — ОКТЯБРЬ 2019
V. 86, N 5 **JOURNAL OF APPLIED SPECTROSCOPY** SEPTEMBER — OCTOBER 2019

ANALYSIS OF PLASMONIC GOLD NANOSTAR ARRAYS WITH THE OPTIMUM SERS ENHANCEMENT FACTOR ON THE HUMAN SKIN TISSUE[**]

S. Golmohammadi[*], M. Etemadi

School of Engineering-Emerging Technologies, University of Tabriz, Tabriz, Iran;
e-mail: sgolmohammadi@tabrizu.ac.ir

We analyze the performance of the surface-enhanced Raman spectroscopy (SERS) substrate based on high-density gold nanostar nanoparticle (GNS) arrays assembled on the gold film and embedded in the human skin tissue as a surrounding medium. A self-assembled monolayer (SAM) of 3-aminopropyltriethoxysilane (APTES) is used for immobilizing GNSs on the Au film. The GNS-Au film and GNS-GNS coupling in the gap regions and also the GNSs interparticle coupling at their branches are observed, so the GNS arrays show more field enhancements and the sensitivity of the GNS sensor can be increased further. When the SERS substrate based on the GNS arrays is excited by a 785 nm laser line, a maximum enhancement factor (EF) of 10^9 is observed. It is demonstrated that the normalized EF depends on the geometry of the GNSs, the thickness of the Au film, and the separation distance between the cores of the GNSs.

Keywords: *nanostars, biomaterials, thin films, surface plasmons, plasmonics, spectroscopy, tissue diagnostics.*

АНАЛИЗ ПЛАЗМОННЫХ НАНОМАТРИЦ ЗОЛОТА С ОПТИМАЛЬНЫМ ФАКТОРОМ УСИЛЕНИЯ ПОВЕРХНОСТНО-УСИЛЕННОГО КОМБИНАЦИОННОГО РАССЕЯНИЯ СВЕТА НА ТКАНИ КОЖИ ЧЕЛОВЕКА

S. Golmohammadi[*], M. Etemadi

УДК 535.375.5;620.3

Школа инженерно-развивающихся технологий, Университет Тебриза, Тебриз, Иран;
e-mail: sgolmohammadi@tabrizu.ac.ir

(Поступила 31 июля 2018)

Методом поверхностно-усиленной спектроскопии комбинационного рассеяния света (SERS) проанализированы свойства подложек, образованных массивами наночастиц золота в виде звезд (GNS), ассамблированных на пленке золота и внедренных в ткани кожи человека. Для иммобилизации GNS на пленке Au использован самоассамблированный монослой 3-аминопропилтриэтоксисилана. Обнаружена связь наночастиц с пленкой и между собой, вследствие чего массивы GNS продемонстрировали большее усиление поля, причем чувствительность сенсоров на основе GNS в дальнейшем может быть увеличена. При возбуждении подложки на основе матриц GNS лазерным излучением с λ = 785 нм наблюдался максимальный коэффициент усиления SERS EF = 10^9. Показано, что нормированный EF зависит от геометрии GNS, толщины пленки Au и расстояния между центрами GNS.

Ключевые слова: *нанозвезды, биоматериал, тонкая пленка, поверхностный плазмон, плазмоника, спектроскопия, диагностика тканей.*

Introduction. Surface-enhanced Raman spectroscopy (SERS) is a highly sensitive technique. Therefore, SERS is widely used for chemical and biological applications [1]. When the surface of metal nanoparticles (NPs) is excited by light, localized surface plasmon resonances (LSPRs) are produced [2]. LSPRs strongly depend on the size, shape, and dielectric properties of both the substrates and the environment [3].

[**] Full text is published in JAS V. 86, No. 5 (http://springer.com/10812) and in electronic version of ZhPS V. 86, No. 5 (http://www.elibrary.ru/title_about.asp?id=7318; sales@elibrary.ru).

Gold NPs have demonstrated less cellular damage as compared with silver [4–6]. Gold nanostructures with different shapes such as nanospheres [6, 7], nanorods [8], nanocubes [9], nanobipyramids [10], nanocrescent [11], and nanostars [12] have been studied for SERS applications; however, there is special interest in nanoparticles with sharp branches due to their unique tunable optical plasmonic properties. For optical imaging applications, the least spectral range is from 650 to 1350 nm. This region is known as the NIR where light exhibits minimal absorption and deep penetration in the tissue [13–16]. The gold nanostars have shown a strong tunable LSPR peak in the NIR region, which can be changed by tuning the size and shape of the branches [17–19]. The LSPR of the gold nanostar is characterized by the great amplification of the electric field in sharp tips, known as hot spots [20].

In this regard, nanostar particles are one of the most useful nanostructures to be placed on imaging probe tips because of their strong electromagnetic hot spots that are able to improve the imaging resolution [21]. When the size of the GNSs increases, the plasmon resonance peak is enhanced. But GNSs with sizes less than 100 nm can be accumulated selectively in tumors via the well-known enhanced permeability and retention effect owing to the increased leakiness of blood vasculature in tumors [16]. NPs with very large diameters are potentially hazardous to human health. Therefore, the best and regular size of the GNSs for optical imaging applications is around 80 nm [17, 20].

One of the important characteristics of SERS is the chemical enhancement factor (EF). EF is the magnitude of increasing the Raman scattering cross section when the molecule is adsorbed on a SERS active substrate [22]. The EF maximum for the single nanosphere is about six orders of magnitude (10^6) [22–24]. For a single nanostar with the branch shape located on the tips, a SERS EF of the 7th order of magnitude (10^7) has been demonstrated, and it is better than the other NPs (for example, nanospheres [6, 25]). The SERS EF increases in nanoclusters such as dimer and trimer, and a number of studies on the SERS of NPs aggregated in the form of nanoclusters have been reported [26–30]. For a single dimer or trimer, the EF is reported to be up to eight orders of magnitude (10^8) under 785 nm illumination [31]. The aggregated solution typically contains an ensemble of monomers and multimers. Therefore, control of the NPs aggregation remains difficult [32, 33]. In the absence of clusters and aggregats, the morphology and density of the GNSs play a more important role in the SERS EF [1, 20, 34].

We represent a GNS array assembled on the Au film and embedded in the human skin tissue. As we know, the metallic NPs and the plasmonic surface can produce LSPR. When these objects are very close to each other, the E-fields are strongly affected by the particle-substrate plasmon coupling and interparticle coupling of high-density NPs [35–37]. The positive interference between their surface plasmons can create a huge field intensity in the hot spot inside the gap [20, 38]. The typical size of the gap is a few nanometers or even less. We have employed a finite difference time domain (FDTD) calculation for the analysis of the optical properties of the structures. Calculation of the SERS EF of the GNS array shows that the normalized EF is strongly affected by the GNSs morphologies, thickness of the Au substrate, and distance between the GNSs.

Simulation details. We simulate the GNSs arrays embedded in the human skin tissue using the FDTD method. The GNS dielectric constant is taken from the paper of Johnson and Christy [39]. The GNS array is excited by a linearly polarized plane wave of 785 nm wavelength having a 1 V/m intensity. This choice is due to the achievement of the best signal-to-noise ratio for the GNS array at 785 nm [40, 41]. The refractive index of the human skin tissue n_{hs} is modeled by the Cornu dispersion equation [42, 43]:

$$n_{\text{hs}} = 1.2573 + 4.5383\times10^2/(\lambda - 2.8745\times10^3), \quad (1)$$

where λ is the incident light wavelength, nm. For the assembly of GNSs on the Au substrate, we use the self-assembled monolayer of APTES. The refractive index of APTES is assumed as [44, 45] $n_{\text{APTES}} = 1.465$.

As previously mentioned, the interaction between the GNS array and nanostar branches creates a strong local field enhancement in the hot spot inside the gap. To resolve such a tiny gap, we use a mesh size of 0.4 nm around and inside the GNSs. Symmetric and antisymmetric boundaries reused in the y and x directions and a perfectly matched layer (PML) boundary condition for the z direction are used to reduce the simulation time.

Theoretical background. The incident laser beam with a frequency of ω_i excites the NPs surface:

$$E_{\text{inc}} = E_0\cos(2\pi t/\omega_i), \quad (2)$$

where E_0 is the incident laser beam electric field amplitude and the local electric field; E_{loc} is the sum of the incident and dipole fields:

$$E_{\text{loc}} = E_{\text{inc}} + E_{\text{d}}. \quad (3)$$

Here the dipole field can be represented as

$$P_i = \propto_i E_\mathrm{d}, \tag{4}$$

where the $\propto_i$ is the polarizability operator and P_i is the dipole moment. EFs depend on the local and incident electric field as described in [46]:

$$\mathrm{EF} = \mathrm{EF}(\omega_i)\mathrm{EF}(\omega_\mathrm{R}), \tag{5}$$

where ω_R is the frequency of the Raman light. The enhancement of the excitation of the Raman active surface at the incident frequency ω_i is given as

$$\mathrm{EF}(\omega_i) = E_\mathrm{loc}(\omega_i)^2/E_0(\omega_i)^2, \tag{6}$$

and the emitted Raman radiation enhancement at the frequency of Raman light is given as follows:

$$\mathrm{EF}(\omega_\mathrm{R}) = E_\mathrm{loc}(\omega_\mathrm{R})^2/E_0(\omega_\mathrm{R})^2. \tag{7}$$

When ω_i and ω_R are very close to each other, Eq. (5) can be rewritten as

$$\mathrm{EF} = \mathrm{E}_\mathrm{loc}(\omega_i)^4/E_0(\omega_i)^4, \tag{8}$$

which brings us back to the well-known fourth-power relationship between the EF and the electric field. Similarly, the ratio between the SERS and the Raman signal intensities can be expressed as

$$I_\mathrm{SERS}/I_\mathrm{Raman} \propto E_\mathrm{loc}(\omega_i)^2/E_0(\omega_i)^2. \tag{9}$$

Since we consider the high-density GNS square array assemblies on the Au film, the SERS EFs are strongly affected by the GNS-substrate interaction and GNS-GNS coupling in the gap regions. In the square array four hot spots from the GNS-Au film coupling and one hot spot from the GNS-GNS coupling participate in the normalized EF of the GNS arrays. Therefore, in order to calculate the EF of the GNS arrays, we use the Jiwon et al. normalized EF formula [20]:

$$\mathrm{EF} = [4|E_\mathrm{loc}/E_0|^4{}_\mathrm{GNS\text{-}substrate} + |E_\mathrm{loc}/E_0|^4{}_{\mathrm{GNS\text{-}GNS}}\omega_i)^2]\times\mathrm{GNS\ surface\ density}. \tag{10}$$

SERS substrate synthesis and assemblies. To investigate the effects of the GNS morphology on the EF and the detection sensitivity, GNS substrates with different sizes and shapes are simulated. The GNS synthesis is difficult and for some cases impractical. Due to the use of the surfactant-free synthesis model, our GNSs can be synthesized by experimental methods. We have simulated GNSs synthesized by the surfactant-free nanostar synthesis model presented by Vo-Dinh et al. [17]. Briefly, 1 M of HCl, 1 mM of $HAuCl_4$, and 6.25 μL of 12 nm citrate-capped spheres (absorbance $A = 3.21$) are mixed by stirring at room temperature and then 50 μL of 100 mM ascorbic acid and 200 μL of 3 mM are added simultaneously and stirred for 5 min. Then a centrifugal wash at 3000–5000 rcf for 15 min is performed, and GNS-3 is filtered by a 0.22 μM nitrocellulose membrane and then refrigerated until further use. To obtain GNSs of similar sizes but of different geometries, we can utilize multiple methods, including different concentration ratios of $AgNO_2$, $HAuCl_4$, and seed, so GNSs with different AR and plasmonic properties are obtained. In particular, the same procedure is followed with 25 μL of seeds to synthesize GNS-2 and with 10 mL of 0.5 mM $HAuCl_4$ to synthesize GNS-1. GNSs are attached on the Au film with APTES amine and silane groups (as can be seen in Fig. 1), so silanization with amino functional groups is carried out by vertically soaking the slides in 5% APTES solution in ethanol at 40°C for 6 h to form a self-assembled monolayer (SAM) followed by thorough rinsing and air drying.

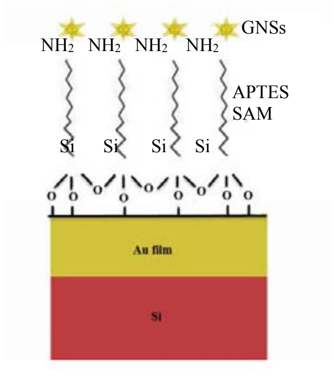

Fig. 1. Scheme of GNSs assembly on the Au film by SAM of APTES. The GNSs are attached on Au film by amine and silane groups of APTES.

Results and discussion. Figure 2a shows a scheme of GNS array assemblies on the 50 nm Au film on top of the Si substrate, embedded in the human skin tissue. The GNSs are attached on the Au film with APTES amine and silane groups with SAM. The separation distance between the GNSs was set to be $d \sim 100$ nm. This wide gap is chosen in order to decrease the strong near-field interaction between the GNSs. GNSs assemble on the Au film with a surface density of ~38 nanoparticles per μm^2. We utilize Si substrates with a higher permittivity, which produce a large field enhancement and exhibit a larger SERS EF [20, 47]. The enhanced Raman signal strength of the GNSs is dependent on multiple factors, such as the GNS concentration on the substrate, the shape, the permittivity of substrates, and the properties of the surrounding medium. In this paper, to investigate the effect of the GNS morphology on the EF and thereby on the detection sensitivity, GNSs with different sizes are simulated. Under 785 nm laser illumination, a strong SERS signal from the GNS array is detected. Figure 2b illustrates a 3D 12-branch GNS schematically. Here R, L, H, and W show the core diameter, the base length, the branch height, and the branch base width, respectively. The aspect ratio is defined as AR = H/W. For achieving different ARs, we fix $R = 32$ nm and $W = 11$ nm as constants and vary H from 14.4 to 33 nm with a 2.2 nm step, so, the value of the AR varies from 1.4 to 3 and L varies from 62.8 nm for AR = 1.4 to 98 nm for AR = 3 with a 4.4 nm step.

The GNS arrays with maximum absorbance peaks at 590 (GNS-1), 700 (GNS-2), and 800 nm (GNS-3) are simulated. Figure 3a shows these GNSs having a difference in the core diameter, the branch number, and the branch aspect ratio (sharpness of the branches). In Fig. 3b the absorption spectra for three different GNS arrays embedded in the human skin tissue are shown.

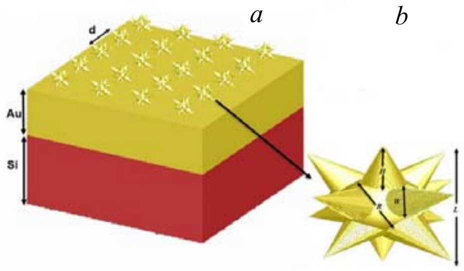

Fig. 2. Schematic description of the simulation of GNS array substrate. (a) Schematic representation of GNS array assemblies on the 50 nm Au film and the Si substrate; (b) schematic diagram of the GNS with morphological parameters: core diameter (R), base length (L), branch height (H), and branch base width (W).

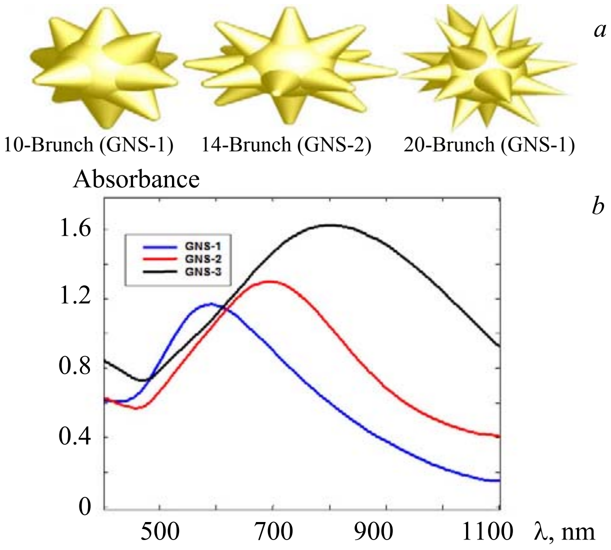
10-Brunch (GNS-1) 14-Brunch (GNS-2) 20-Brunch (GNS-1)

Fig. 3. GNSs with different morphology and characteristic absorption spectra. (a) Simulated scheme and (b) FDTD-simulated absorption spectra of the GNSs excited with 785 nm incident radiation.

TABLE 1. Structural Parameters of GNS-1, GNS-2, and GNS-3

Gold nanostar	Branch number	Core diameter *R*, nm	Branch height *H*, nm	Branch base width *W*, nm
GNS-1	10	36	21	18
GNS-2	14	40	20	14
GNS-3	20	45	18	10

The GNSs with different morphologies are simulated (see Table 1). GNS-3 possesses more branches with high sharpness, while GNS-1 has relatively few branches and less sharp branches. It should be noted that the three cited GNS sizes are equal to ~80±3 nm. GNS hot spots increase by increasing the branch number of GNSs, and a large field enhancement occurs at these points. Figure 4 shows the FDTD simulation results for the *E*-field distribution of GNS assemblies on the Au film. Because of the higher density of the GNS array assemblies on the Au film, the SERS EF is strongly affected by the GNS-Au film interaction, the GNS-GNS coupling in the gap regions, and the GNSs interparticle coupling at their branches.

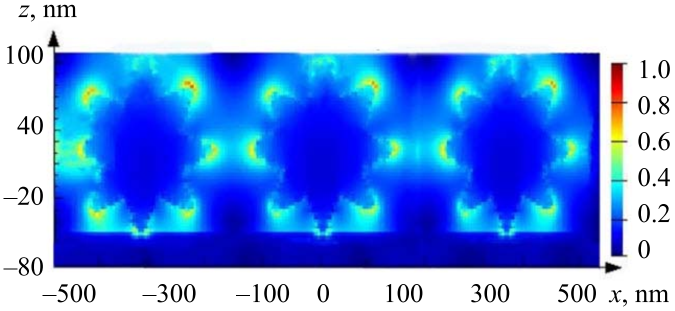

Fig. 4. FDTD simulation of E-field of the GNS arrays assembled on Au film and embedded in human skin.

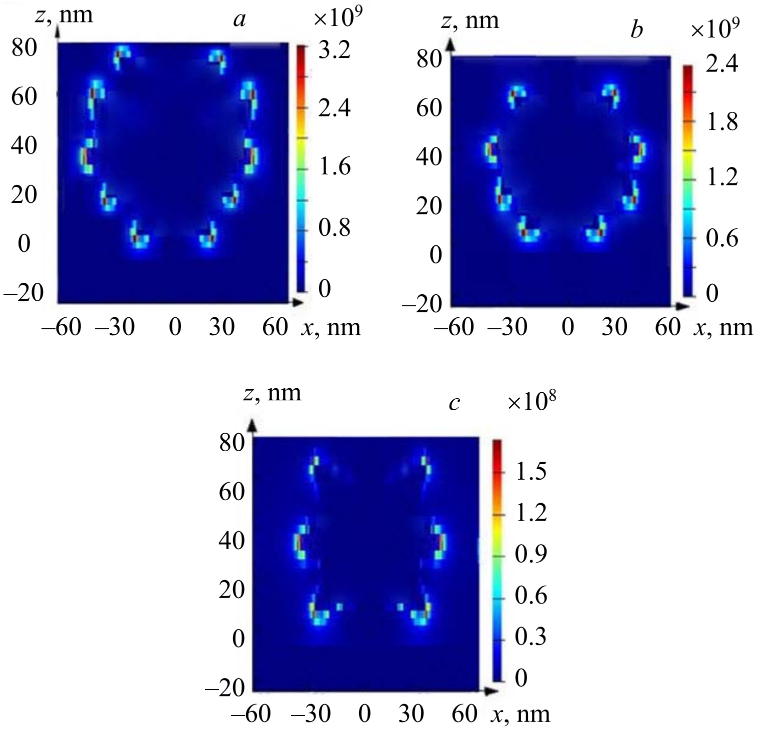

Fig. 5. Comparison between the EF of the GNS array with different morphologies embedded in the human skin tissue. The *xz*-EF of the GNS-3 (a), GNS-2 (b), and GNS-1 (c). The wavelength of excited laser beam is 785 nm.

The SERS EFs for GNS substrates with different morphologies are calculated by Eq. (9). For substrates GNS-1, GNS-2, and GNS-3 the average SERS EFs are 6.8×10^8. 2.1×10^9, and 5.6×10^9, respectively. Figure 5 shows a comparison between the SERS EF for GNSs with different morphologies. GNS-3 shows a higher EF in comparison with GNS-2 and GNS-1. The reason for this is that GNS-3 (Fig. 5a) possesses more and sharper branches than GNS-2 and GNS-1 (Fig. 5b,c). In addition, the maximum absorbance peak of GNS-3 (800 nm) is very close to the laser excitation wavelength (785 nm), so this resonance causes a significant EF for GNS-3 [17, 34].

Figure 6 shows the normalized EF as a function of the GNS-3′s branch AR, the core diameter, and the branch number. As previously mentioned, AR is the ratio of the branch height to the branch base width, so branches of the GNSs become longer and sharper by increasing the AR. As can be seen in Fig. 6a, the LSPR peak of the GNSs is red-shifted. However, the intensity of the LSPR peak is decreased. Since the plasmon peak position is red-shifted for larger ARGNSs, the sharper branches interact less intensely with the NIR laser excitation (785 nm) [17, 34], and this can cause less enhancement of the normalized EF (Fig. 6b).

As shown in Fig. 6c, by increasing the core diameter of GNS, the plasmon peak intensity increases in the NIR region, and the LSPR peak is shifted to the shorter wavelengths (a blue shift occurs) [17], and multiple LSPRs with respect to the tips and core-tip interactions are monitored. At first, for a core diameter below ~65 nm, with increasing the core diameter the normalized EF of the GNSs increases (Fig. 6d). For a core diameter much larger than the branch height, GNS becomes like a nanosphere, and core-tip interactions decrease; the normalized EF decreases (Fig. 6d).

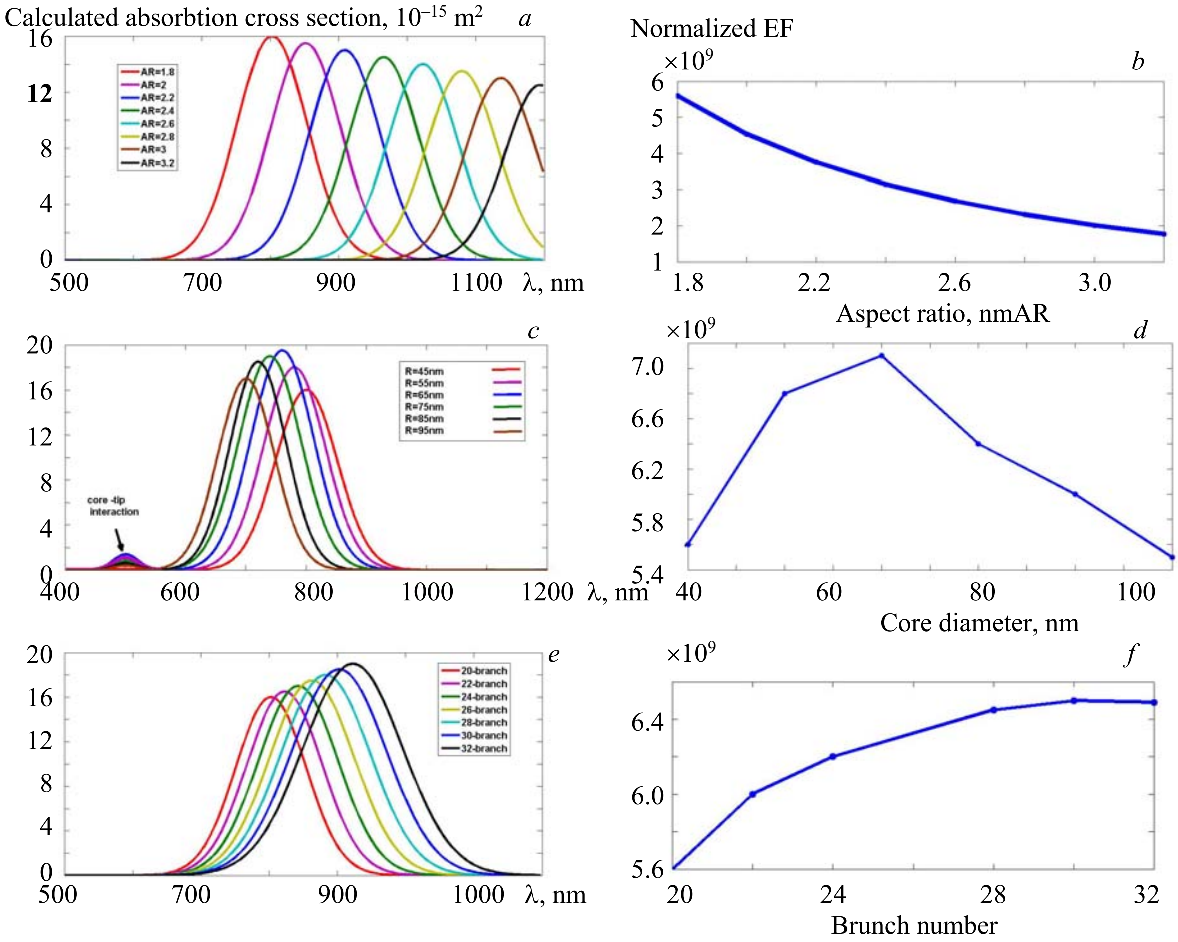

Fig. 6. Calculated absorption spectra (a) and normalized EF (b) of the GNS-3 array embedded in the human skin tissue as a function of the branch AR; calculated absorption spectra (c) and the normalized EF (d) of the GNS-3 array embedded in the human skin tissue as a function of the core diameter; calculated absorption spectra (e) and normalized EF (f) of the GNS-3 array embedded in the human skin tissue as a function of the branch number.

With increasing the GNS branch number, the number of hot spots increases, too [16, 17]. As can be seen in Fig. 6e, the LSPR peak increases and is shifted to the NIR region. Thus, the resonance between the plasmon peak of the GNSs, the laser excitation wavelength, and the branch hot spots cause more enhancement in the normalized EF (Fig. 6f).

To investigate the effect of different interparticle separations between the GNSs (*d* in Fig. 2a) on the normalized EF, we simulate a GNS-3 array on the 60 nm Au film. The interparticle separation distance is considered as the distance between the cores of GNSs. Since the surface of the Au film remains unchanged and equal to 1000×1000 nm, the surface density of the GNSs on the Au film decreases by increasing the separation distance between the GNSs. At first, for an interparticle separation below ~50 nm by increasing the separation distance between the GNSs, the normalized EF is increased (Fig. 7a). This behavior can be explained by studying the interaction between the GNS-GNS and GNS-Au film couplings. When the interparticle separation is below ~50 nm, the GNS-GNS coupling is strong and the GNS-Au film coupling becomes weak (Fig. 7b). Therefore, the interaction between them will increase the normalized EF.

For an interparticle separation over ~50 nm, since the GNS-GNS coupling, which depends on the interparticle separation, becomes weak, the GNS-Au film coupling is more effective (Fig. 7b). Meanwhile, the normalized EF is decreased.

When the interparticle separation between the GNSs is about ~50 nm, and the surface density of the GNS-3 arrays is constant and equal to ~64 GNS/μm^2, the normalized EF is decreased by increasing the thickness of the Au film (Fig. 7c). By increasing the thickness of the Au film, the permittivity of this film becomes low [48], and the GNS–Au film coupling, which depends on the Au film permittivity, is more effective than the GNS–GNS coupling for the normalized EF. For thicker Au films, the GNS–Au film coupling and GNS–GNS coupling becomes low (Fig. 7d). Consequently, the normalized EF is decreased. Due to the difficulty in synthesizing the thinner Au film, we used the 60 nm Au film as the substrate.

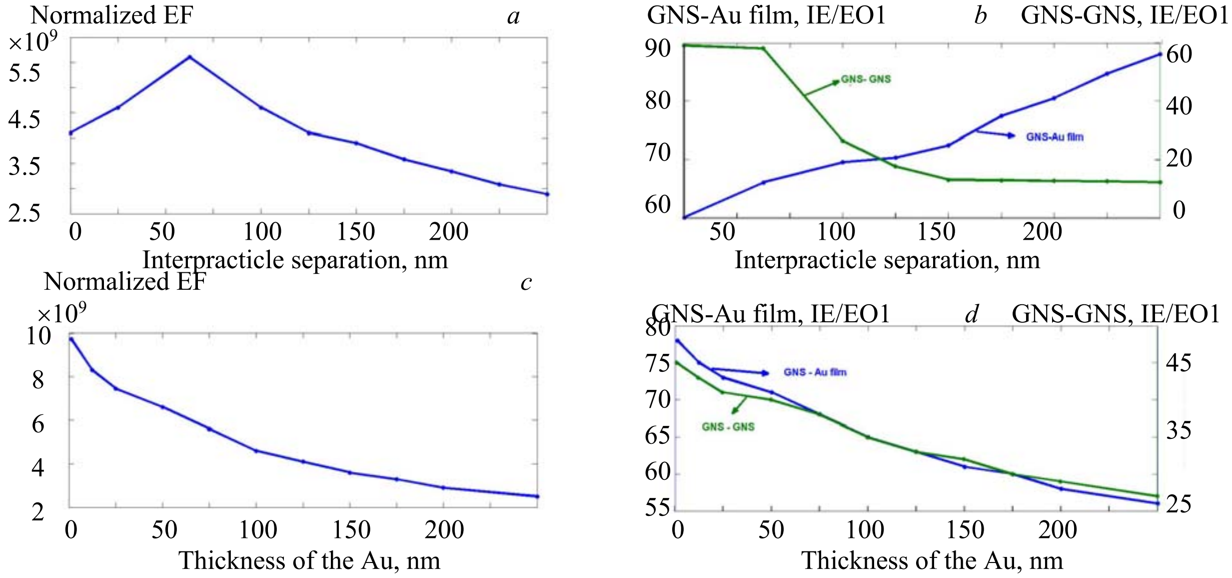

Fig. 7. Normalized EF for GNS-3 array embedded in the human skin (a) and local E-field enhancement from GNS–Au film and GNS–GNS plasmon coupling via interparticle separation (b) when the surface density of the GNSs varies from 12 to 72 GNS/μm^2; the normalized EF for GNS-3 array embedded in the human skin (c) and local E-field enhancement from GNS–Au film and GNS–GNS plasmon coupling as a function of the thickness of the Au film (d) when the interparticle separation is ~50 nm.

A strong signal from GNS-3 on the SERS substrate inside the human skin tissue is observed. In the presence of higher density of GNSs in the human skin tissue, the electric field distribution becomes very high inside the human skin because of the GNSs acting as the focusing points [41]. High permittivity media also provide stronger image charges and thus larger interaction with the localized surface plasmons of the GNSs [20]. Therefore, the human skin tissue exhibits a larger SERS EF than air (Fig. 8). The SERS substrates based on high-density GNS arrays in the human skin tissue gives a better performance in comparison with the air. Therefore, it is suitable for intracellular sensing and imaging [49, 50].

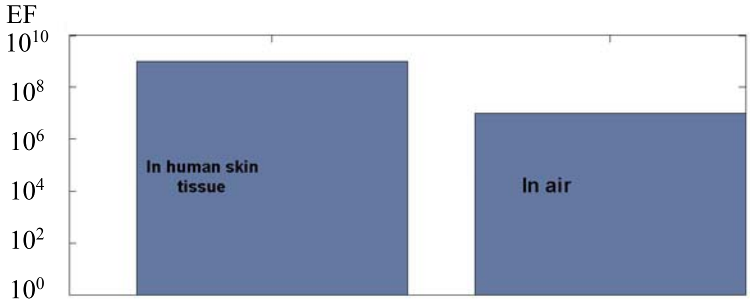

Fig. 8. Comparison between the EF of the GNS-3 array assemblies on the 60 nm Au film with an interparticle separation of ~50 nm and embedded in the human skin and air media.

Conclusion. We studied the performance of the SERS substrate based on high-density GNS arrays for intracellular sensing and imaging. We analyzed the performance of the GNS arrays embedded in the human skin tissue and air. We established that the high-density GNSs arrays on the Au film are characterized by a high SERS EF dependent on the interactions of the GNS-Au film, GNS-GNS in the gap regions, and the GNSs at their branches. In this paper, we compared the normalized EF for the GNSs with different morphologies and different surrounding media. As a result, we showed that the proposed SERS substrates possess great potential in intracellular imaging, medical diagnostics, and therapy. We demonstrated that by increasing the branch number of the GNSs the normalized EF of the GNS arrays on the Au film increases. However, the normalized EF of the GNS arrays on the Au film decreases as a function of the branch aspect ratio (AR). We also observed that for a core diameter below ~65 nm, by increasing this diameter the normalized EF of the GNSs increased, and for a core diameter over ~65 nm by increasing this diameter the EF decreased. Finally, we investigated the impact of the Au film thickness and the distance between the cores of the GNSs on the SERS EF. It is found that the normalized EF decreases by increasing the thickness of the Au film, and for a distance of ~50 nm between GNSs cores the SERS substrate is characterized by a larger normalized EF.

REFERENCES

1. L. Osinkina, T. Lohmuller, F. Jackel, J. Feldmann, *J. Phys. Chem. C*, **117**, 22198–22202 (2013).
2. T. Vo-Dinh, A. M. Fales, G. D. Griffin, C. G. Khoury, Y. Liu, H. Ngo, S. J. Norton, J. K. Register, H.-N. Wang, H. Yuan, *Nanoscale*, **5**, 10127–10140 (2013).
3. K. L. Kelly, E. Coronado, L. L. Zhao, G. C. Schatz, *The Optical Properties of Metal Nanoparticles: The Influence of Size, Shape, and Dielectric Environment*, ACS Publications (2003).
4. E. Boisselier, D. Astruc, *Chem. Soc. Rev.*, **38**, 1759–1782 (2009).
5. M. V. Park, A. M. Neigh, J. P. Vermeulen, L. J. de la Fonteyne, H. W. Verharen, J. J. Briedé, H. van Loveren, W. H. de Jong, *Biomaterials*, **32**, 9810–9817 (2011).
6. G. Bisker, D. Yelin, *J. Opt. Soc. Am. B*, **29**, 1383–1393 (2012).
7. M. Yang, X. Yang, L. Huai, *Appl. Phys. A: Mater. Sci. Process*., **92**, 367–370 (2008).
8. T. Pylaev, V. Khanadeev, B. Khlebtsov, L. Dykman, V. Bogatyrev, N. Khlebtsov, *Nanotechnology*, **22**, 285501 (2011).
9. B. Khlebtsov, V. Khanadeev, I. Maksimova, G. Terentyuk, N. Khlebtsov, *Nanotechnol. Russ.*, **5**, 454–468 (2010).
10. M. Liu, P. Guyot-Sionnest, *J. Phys. Chem. B*, **109**, 22192–22200 (2005).
11. G. P. Kumar, *J. Opt. Soc. Am. B*, **29**, 594–599 (2012).
12. C. L. Nehl, H. Liao, J. H. Hafner, *Nano Lett.*, **6**, 683–688 (2006).
13. H. Yockell-Lelièvre, F. Lussier, J.-F. Masson, *J. Phys. Chem. C*, **119**, 28577–28585 (2015).
14. N. Li, P. Zhao, D. Astruc, *Angew. Chem. Int. Ed*., **53**, 1756–1789 (2014).
15. A. H. Gandjbakhche, *Compt. Rend. Acad. Sci., Ser. IV Phys.*, **2**, 1073–1089 (2001).

16. Y. Liu, H. Yuan, F. R. Kersey, J. K. Register, M. C. Parrott, T. Vo-Dinh, *Sensors*, **15**, 3706–3720 (2015).
17. H. Yuan, C. G. Khoury, H. Hwang, C. M. Wilson, G. A. Grant, T. Vo-Dinh, *Nanotechnology*, **23**, 075102 (2012).
18. P. Yang, J. Zheng, Y. Xu, Q. Zhang, L. Jiang, *Adv. Mater.*, **28**, 10508–10517 (2016).
19. T. K. Lee, S. K. Kwak, *J. Phys. Chem. C*, **118**, 5881–5888 (2014).
20. J. Lee, B. Hua, S. Park, M. Ha, Y. Lee, Z. Fan, H. Ko, *Nanoscale*, **6**, 616–623 (2014).
21. H. Yuan, J. K. Register, H.-N. Wang, A. M. Fales, Y. Liu, T. Vo-Dinh, *Anal. Bioanal. Chem.*, **405**, 6165–6180 (2013).
22. P. L. Stiles, J. A. Dieringer, N. C. Shah, R. P. Van Duyne, *Annu. Rev. Anal. Chem.*, **1**, 601–626 (2008).
23. M. Kerker, D.-S. Wang, H. Chew, *Appl. Opt.*, **19**, 3373–3388 (1980).
24. J. Z. Zhang, *J. Phys. Chem. Lett.*, **1**, 686–695 (2010).
25. C. Hrelescu, T. K. Sau, A. L. Rogach, F. Jäckel, J. Feldmann, *Appl. Phys. Lett.*, **94**, 153113 (2009).
26. J. Hu, P.-C. Zheng, J.-H. Jiang, G.-L. Shen, R.-Q. Yu, G.-K. Liu, *Analyst*, **135**, 1084–1089 (2010).
27. Z. Zhang, Y. Wen, Y. Ma, J. Luo, X. Zhang, L. Jiang, Y. Song, *Appl. Phys. Lett.*, **98**, 133704 (2011).
28. P. Taladriz-Blanco, N. J. Buurma, L. Rodríguez-Lorenzo, J. Pérez-Juste, L. M. Liz-Marzán, P. Hervés, *J. Mater. Chem.*, **21**, 16880–16887 (2011).
29. A. Saha, S. Palmal, N. R. Jana, *Nanoscale*, **4**, 6649–6657 (2012).
30. L. Fabris, M. Dante, T. Q. Nguyen, J. B. H. Tok, G. C. Bazan, *Adv. Funct. Mater.*, **18**, 2518–2525 (2008).
31. S. L. Kleinman, B. Sharma, M. G. Blaber, A.-I. Henry, N. Valley, R. G. Freeman, M. J. Natan, G. C. Schatz, R. P. Van Duyne, *J. Am. Chem. Soc.*, **135**, 301–308 (2012).
32. J. M. Romo-Herrera, R. A. Alvarez-Puebla, L. M. Liz-Marzán, *Nanoscale*, **3**, 1304–1315 (2011).
33. J.-H. Lee, J.-M. Nam, K.-S. Jeon, D.-K. Lim, H. Kim, S. Kwon, H. Lee, Y. D. Suh, *ACS Nano*, **6**, 9574–9584 (2012).
34. A. D. S. Indrasekara, S. Meyers, S. Shubeita, L. Feldman, T. Gustafsson, L. Fabris, *Nanoscale*, **6**, 8891–8899 (2014).
35. H. R. Stuart, D. G. Hall, *Phys. Rev. Lett.*, **80**, 5663 (1998).
36. P. Nordlander, C. Oubre, E. Prodan, K. Li, M. Stockman, *Nano Lett.*, **4**, 899–903 (2004).
37. A. Kravets, T. Borodinova, V. Kravets, *J. Opt. Soc. Am. B*, **33**, 302–307 (2016).
38. S. Piltan, D. Sievenpiper, *J. Opt. Soc. Am. B*, **35**, 208–213 (2018).
39. P. B. Johnson, R.-W. Christy, *Phys. Rev. B*, **6**, 4370 (1972).
40. A. Shiohara, S. M. Novikov, D. M. Solís, J. M. Taboada, F. Obelleiro, L. M. Liz-Marzán, *J. Phys. Chem. C*, **119**, 10836–10843 (2014).
41. F. Tian, J. Conde, C. Bao, Y. Chen, J. Curtin, D. Cui, *Biomaterials*, **106**, 87–97 (2016).
42. H. Ding, J. Q. Lu, W. A. Wooden, P. J. Kragel, X.-H. Hu, *Phys. Med. Biol.*, **51**, 1479 (2006).
43. T. Lister, P. A. Wright, P. H. Chappell, *J. Biomed. Opt.*, **17**, 0909011–09090115 (2012).
44. J. Le Grange, J. Markham, C. Kurkjian, *Langmuir*, **9**, 1749–1753 (1993).
45. J. A. Howarter, J. P. Youngblood, *Langmuir*, **22**, 11142–11147 (2006).
46. S. Atta, T. V. Tsoulos, L. Fabris, *J. Phys. Chem. C*, **120**, 20749–20758 (2016).
47. Q.-Q. Meng, X. Zhao, C.-Y. Lin, S.-J. Chen, Y.-C. Ding, Z.-Y. Chen, *Sensors*, **17**, 1846 (2017).
48. A. Kossoy, V. Merk, D. Simakov, K. Leosson, S. Kéna-Cohen, S. A. Maier, *Adv. Opt. Mater.*, **3**, 71–77 (2015).
49. M. W. Knight, Y. Wu, J. B. Lassiter, P. Nordlander, N. J. Halas, *Nano Lett.*, **9**, 2188–2192 (2009).
50. S.-Y. Chen, J. J. Mock, R. T. Hill, A. Chilkoti, D. R. Smith, A. A. Lazarides, *ACS nano*, **4**, 6535–6546 (2010).